The Development of Simulated Dust-Devil-Like Vortices

JOHANNES M. L. DAHL[a]

[a] *Atmospheric Science Group, Department of Geosciences, Texas Tech University, Lubbock, Texas*

(Manuscript received 5 December 2023, in final form 16 August 2024, accepted 23 August 2024)

ABSTRACT: In this study, the cause of rotation in simulated dust-devil-like vortices is investigated. The analysis uses a numerical simulation of an initially resting, dry, atmosphere, in which uniform surface heating leads to the development of a growing convective boundary layer (CBL). As soon as convective mixing sets in, regions of weak vertical vorticity develop at the lowest model level. Using forward trajectories, this vorticity is shown to originate from horizontal baroclinic production and simultaneous reorientation into the vertical within the descending branches of the convective cells. The requirement for vertical vorticity production in the downdraft cells is shown to be a nonaxisymmetric horizontal footprint of the downdraft regions. The resulting vertical vorticity is not initially associated with rotation. However, as the CBL matures, like-signed vortex patches merge, the vertical vorticity magnitude increases due to stretching, and deformation in the vortex patch decreases, leading to the development of vortices. The ultimate origin of the vortices is thus initially horizontal vorticity that has been produced baroclinically and that has subsequently been reoriented into the vertical in sinking air.

SIGNIFICANCE STATEMENT: Dust devils are concentrated vortices consisting of rapidly rising buoyant air, which may pose a risk to small aircraft and light structures on the ground. Although these vortices are a common occurrence in convective boundary layers, the origin of the vorticity within these vortices has not yet been fully established. The present study uses a numerical simulation of an evolving convective boundary layer and analyzes air parcel trajectories to identify the origin of vertical vorticity at the surface during dust-devil formation. The work contributes an answer to the long-standing question of what causes dust devils to spin.

KEYWORDS: Atmosphere; Boundary layer; Vortices; Numerical analysis/modeling

1. Introduction

Dust devils have long been known to accompany convectively mixed boundary layers (e.g., Kanak et al. 2000). As reviewed by, e.g., Rafkin et al. (2016), the general requirement for dust devils is a superadiabatic surface layer, relatively weak background winds, and relatively flat terrain; these conditions are conveniently described by the Obukhov length scale (Hess and Spillane 1990), the smallness of which (in magnitude) signifies the degree to which these conditions are met (e.g., Kurgansky et al. 2011). However, to the author's knowledge, the details of how dust devils initially acquire their rotation have not been completely documented in the formal literature.

Ohno and Takemi (2010) analyzed the different terms in the vertical vorticity equation for a fully developed, simulated dust devil within a convective boundary layer (CBL) and found that the tilting and stretching terms were large at the base of the vortex analyzed in that study. Raasch and Franke (2011) likewise found that the tilting and stretching terms were dominant at the base of their simulated vortices. A limitation of these studies is that only the vertical vorticity equation was considered, such that the origin of the vorticity that was tilted and stretched could not be established. Ito et al. (2013) considered the circulation budget of material surfaces for a simulated dust devil within a CBL, and they described how the material surface contracted horizontally while also becoming increasingly level as it approached the vortex, consistent with the tilting and stretching of vorticity. The relatively short integration period (128 s) did not allow Ito et al. (2013) to identify the source of the circulation, although they noticed that circulation is maximized in downdraft regions. In addition, they inferred that the ultimate source of rotation is likely baroclinically produced horizontal vorticity that is reoriented by vertical-velocity gradients due to the convective circulations. In fact, as pointed out by Fiedler and Kanak (2001), within a domain initially devoid of any vorticity, baroclinic production is the only source of rotation (along with horizontal vorticity produced at the lower domain boundary). However, even if it is accepted that the ultimate cause of vorticity in dust devils is horizontal baroclinic production associated with the convective cells in the boundary layer, the question arises of how this horizontal vorticity leads to vertical vorticity at the ground where it is needed for dust-devil formation.[1]

The need for downdrafts

Carroll and Ryan (1970) were perhaps the first to speculate that downdrafts are ultimately responsible for the production

---

Denotes content that is immediately available upon publication as open access.

Corresponding author: Johannes Dahl, johannes.dahl@ttu.edu

[1] Technically, the flow and its vertical vorticity is zero at $z = 0$ due to the no-slip condition; here "surface-level" or "ground-level" rotation refers to arbitrarily small heights above the ground.

DOI: 10.1175/JAS-D-23-0228.1

of surface vertical vorticity in the convective boundary layer. The requirement for downdrafts in producing ground-level rotation in the absence of preexisting vertical vorticity has been highlighted in the field of tornado research (e.g., Davies-Jones 1982; Davies-Jones and Brooks 1993; Walko 1993; Parker and Dahl 2015; Fischer et al. 2024). The main idea is that appreciable vertical vorticity cannot arise at the ground by updraft gradients tilting horizontal vortex lines vertically: As the vorticity is being reoriented vertically, the air rises away from the ground, and consequently significant vertical vorticity only develops some distance above the ground (see also Markowski and Richardson 2010, p. 277; Markowski et al. 2014). While the mechanism by which surface vertical vorticity develops in supercell thunderstorms prior to tornadogenesis is reasonably well understood (Davies-Jones and Brooks 1993; see also Dahl et al. 2014; Markowski and Richardson 2014; Markowski et al. 2014; Parker and Dahl 2015; Fischer et al. 2024), such a mechanism does not seem to have been discussed in the context of boundary layer vortices.

The purpose of this study is thus to revisit the question of where the rotation in numerically simulated dust-devil-like vortices (DDLVs) originates from, focusing on the period prior to the development of fully developed DDLVs. By beginning the analysis when the atmosphere is still at rest, 3D vorticity dynamics along air parcel trajectories can be applied to identify the origin of vertical vorticity at the bottom of the CBL.

2. Method

To simulate the developing convective boundary layer, the Bryan Cloud Model 1 (CM1; Bryan and Fritsch 2002) release 19.5 was utilized. The initial state is a dry resting atmosphere, which is heated from below. The surface is uniform and flat and receives solar radiation corresponding to 34°N, 102°W. The simulation is started at 2000 UTC 15 July 2023 (1500 local time; the reader may skip ahead to the time series in Fig. 10a to see the resulting sensible surface heat flux, $\overline{\theta' w'}$). The computational domain is a $4 \times 4 \times 5\ \mathrm{km}^3$ box, in which the horizontal grid spacing is 10 m throughout, and the vertical grid spacing is 5 m in the lowest 2 km,[2] increasing to 595 m at the domain top. The large model time step is 0.2 s, and there is no Coriolis acceleration in the simulation. A Rayleigh sponge layer was added in the uppermost 2.5 km to avoid reflection of upward propagating gravity waves. The lateral boundary conditions are periodic, and the momentum fluxes at the lower boundary are determined based on Monin–Obukhov similarity theory, using the WRF/MM5 surface layer scheme (Jiménéz et al. 2012). The vertical temperature profile is slightly stable to allow for a reasonably fast deepening of the CBL. The relevant model settings are summarized in Table 1.

The horizontal grid spacing of 10 m is not sufficient to simulate the structure of dust devils faithfully, as demonstrated by, e.g., Spiga et al. (2016) or Giersch and Raasch (2023). However, the focus of this study is on the early stages of vertical vorticity production; at this stage, the vorticity structures are of the scale of the convective cells, which are well resolved at $\Delta x = 10$ m [the reader may skip ahead to Fig. 2 for an example; see also, e.g., Kanak et al. (2000) or Ito et al. (2013)]. However, even at later times, the vortex structures that do develop bear a crude resemblance to analytical models and vortex-scale simulations, including a rudimentary representation of the vortex boundary layer, which is critical to the intensification of these vortices (Rotunno 2013), as discussed further in section 3d.

TABLE 1. Main settings of the CM1 simulation. The variable θ refers to potential temperature.

Model parameter	Setting
nx	408
ny	408
nz	410
dx	10 m
dy	10 m
dz	5 m, increasing to 595 m between 2000 and 5000 m AGL
Domain size	$4080 \times 4080 \times 5000\ \mathrm{m}^3$
Initial random θ perturbations	0.1 K
Base state kinematic profile	Resting
Base state thermodynamic profile	Dry, $\partial\theta/\partial z = 1\ \mathrm{K\ km^{-1}}$
Lower boundary condition	Semi-slip (based on Monin–Obukhov similarity theory)
Pressure solver	Vertically implicit, Klemp and Wilhelmson time-splitting scheme
Advection scheme	Fifth-order (including numerical diffusion)
Turbulence closure	1.5-order TKE scheme (Deardorff 1980)
Surface properties	Barren or sparsely vegetated, summer (roughness length: 1 cm)

The analysis utilizes forward-integrated air parcel trajectories, which are calculated during run time at each large model time step within the CM1 model, using a third-order Runge–Kutta scheme. The advantage of the forward, compared to backward, integration is improved accuracy near confluent flows, such as convective vortices, as discussed by, e.g., Dahl et al. (2012). The momentum tendencies are taken directly from the dynamical core of the model, so that the complete budget of the 3D vorticity equation may be extracted, and subsequently interpolated to the parcel locations. The 3D vorticity equation is given by (e.g., Markowski and Richardson 2010, p. 21)

$$\frac{d\boldsymbol{\omega}}{dt} = \boldsymbol{\omega}\cdot\nabla\mathbf{v} - \boldsymbol{\omega}(\nabla\cdot\mathbf{v}) + \frac{1}{\rho^2}\nabla\rho\times\nabla p + \nabla\times\mathbf{f}_{\mathrm{turb}} + \nabla\times\mathbf{f}_{\mathrm{diff}}, \tag{1}$$

where $\boldsymbol{\omega} = \nabla\times\mathbf{v} = (\xi, \eta, \zeta)$ is the vorticity vector, $\mathbf{v} = (u, v, w)$ is the wind vector, p is the pressure, ρ is the air density, $\mathbf{f}_{\mathrm{turb}}$ is the acceleration due to subgrid-scale (SGS) turbulent mixing,

---

[2] This puts the lowest (u, v) and scalar grid points at 2.5 m AGL.

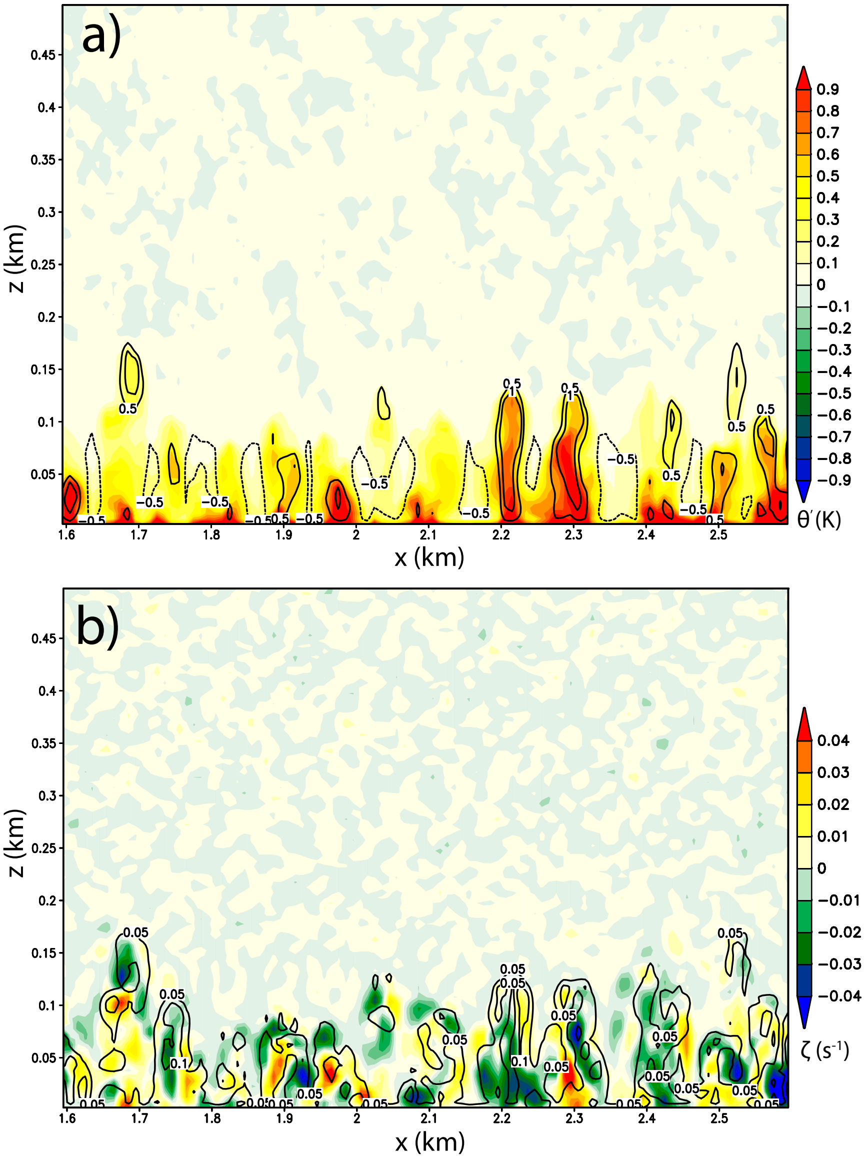

FIG. 1. (a) Vertical cross section ($y = 0.495$ km) of the potential-temperature perturbation (shaded) and vertical velocity [black contours, $(-1, -0.5, 0.5, 1)$ m s^{-1}] at 400 s. (b) Vertical vorticity (shaded) and horizontal vorticity magnitude [black contours, $(-0.1, -0.05, 0.05, 0.1)$ s^{-1}] at 400 s.

and $\mathbf{f}_{\mathrm{diff}}$ is the acceleration due to numerical diffusion. The first two terms on the rhs of Eq. (1) represent the effects of stretching and tilting of the vorticity vector, the third term represents baroclinic vorticity production (e.g., Markowski and Richardson 2010, p. 23), and the last two terms represent vorticity production via differential subgrid-scale and numerical mixing.

3. Results

a. Development of the convective boundary layer and vorticity noise

To trigger convective mixing in the boundary layer, potential temperature (θ) perturbations with a maximum amplitude of 0.1 K were added in the entire domain at the first time step of the simulation. Without such perturbations, no mixing ensues even in the presence of superadiabatic near-surface temperature lapse rates. Interestingly, weak vertical vorticity at the lowest scalar model level (2.5 m AGL) already appears a few seconds after the simulation has started. This development is related to the θ perturbations, which are associated with weak buoyancy perturbations, which result in weak horizontal baroclinically produced circulations. The weak horizontal vorticity thus produced is reoriented and leads to extrema of vertical vorticity on the order of 10^{-4} s^{-1} throughout the domain. The resulting vertical vorticity is an order of magnitude weaker than the vorticity that develops around 400 s into the simulation when convective mixing due to the developing superadiabatic surface layer sets in. Indeed, Fig. 1

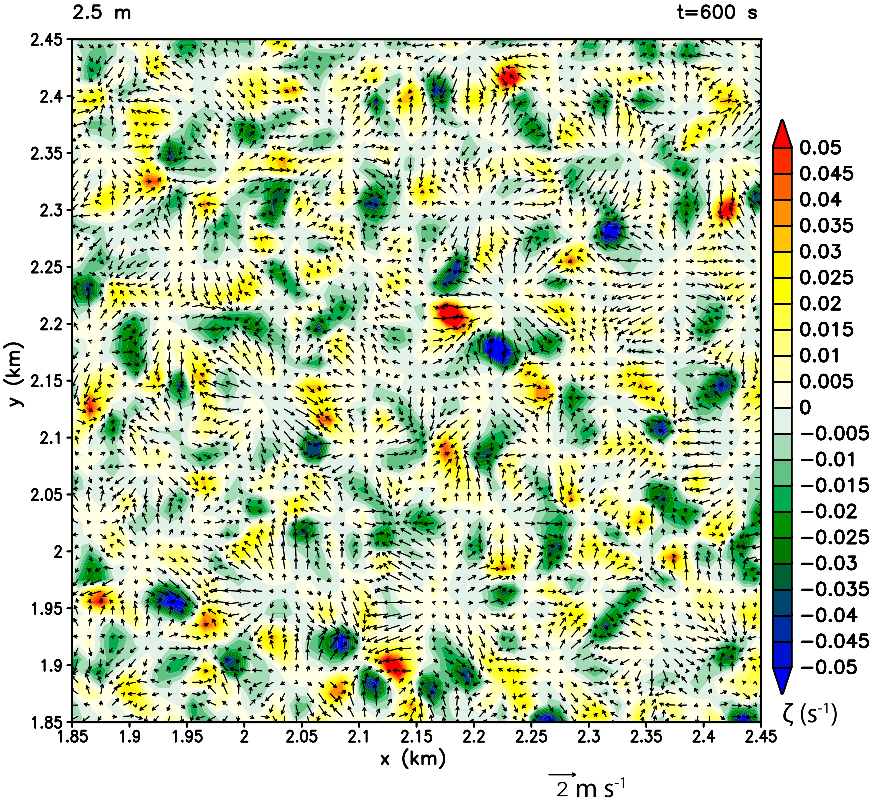

FIG. 2. Vertical vorticity (shaded) and horizontal wind vectors (arrows) at the lowest model level (2.5 m AGL) at 600 s.

shows that the perturbations associated with the convection driven by surface heating is much stronger than the random perturbations, which are visible as weak noise throughout the domain. In other words, the weak initial vertical vorticity is associated with the potential-temperature noise and is not related to the developing convective boundary layer.

b. Early vertical vorticity evolution

The convective structures that develop about 400 s into the simulation are larger and more coherent compared to the random noise (Fig. 1). At that time, a cellular structure appears also in the horizontal plane, and vertical vorticity extrema that mirror this structure emerge (Fig. 2). It is this initial vertical vorticity whose origin is of interest. At this point, the CBL is still in its infancy: Mixing is weak (peak vertical velocities on the order of 0.5 m s^{-1}) and shallow (about 100 m).

To understand this initial development of surface vertical vorticity, 510 050 trajectories were launched at 300-s simulation time in a roughly 500 × 500 × 250 m^3 box in the middle of the domain with an initial horizontal and vertical spacing of 5 m. Only those trajectories were considered that terminated close to the surface (between 2.5 and 5 m AGL) between 599 and 600 s and within a region of weak positive vertical vorticity ($\zeta \geq 0.015$ s^{-1}). These considerations reduced the number of useful parcels to $n = 584$. These trajectories are shown in Fig. 3. The parcels initially rest in the air above the growing CBL at roughly 60 m AGL and at some point are entrained into the CBL, with most parcels simply descending to the ground (others first rise and then descend). To analyze vorticity budgets, parcels were discarded if they descended below the lowest scalar model level, as the horizontal winds are not defined there (e.g., Vande Guchte and Dahl 2018). Moreover, the integrated vorticity budgets had to match the interpolated vorticity reasonably well; this determination was made subjectively (but in an automated manner, by filtering trajectories based on the accumulated absolute error of the integrated vorticity). Only about a dozen parcels remained after this procedure ($n = 11$), which are shown in black in Fig. 3.

First, the horizontal vorticity budgets along the trajectories are considered. These may be inferred by integrating the equation for the horizontal vorticity magnitude (e.g., Boyer and Dahl 2020):

$$\frac{d|\boldsymbol{\omega}_h|}{dt} = \mathbf{s} \cdot \frac{d\boldsymbol{\omega}_h}{dt}, \qquad (2)$$

where $\boldsymbol{\omega}_h$ is the horizontal vorticity vector and $d\boldsymbol{\omega}_h/dt$ is given by the x and y components of Eq. (1). The unit vector $\mathbf{s}$ is tangent to the local vortex lines (i.e., $\mathbf{s} = \boldsymbol{\omega}_h/|\boldsymbol{\omega}_h|$).

Figure 4a shows the different integrated terms of Eq. (2) for the average parcel. Perhaps not surprisingly, baroclinic production is the dominant contribution in the horizontal vorticity budget. Moreover, the parcels are descending while

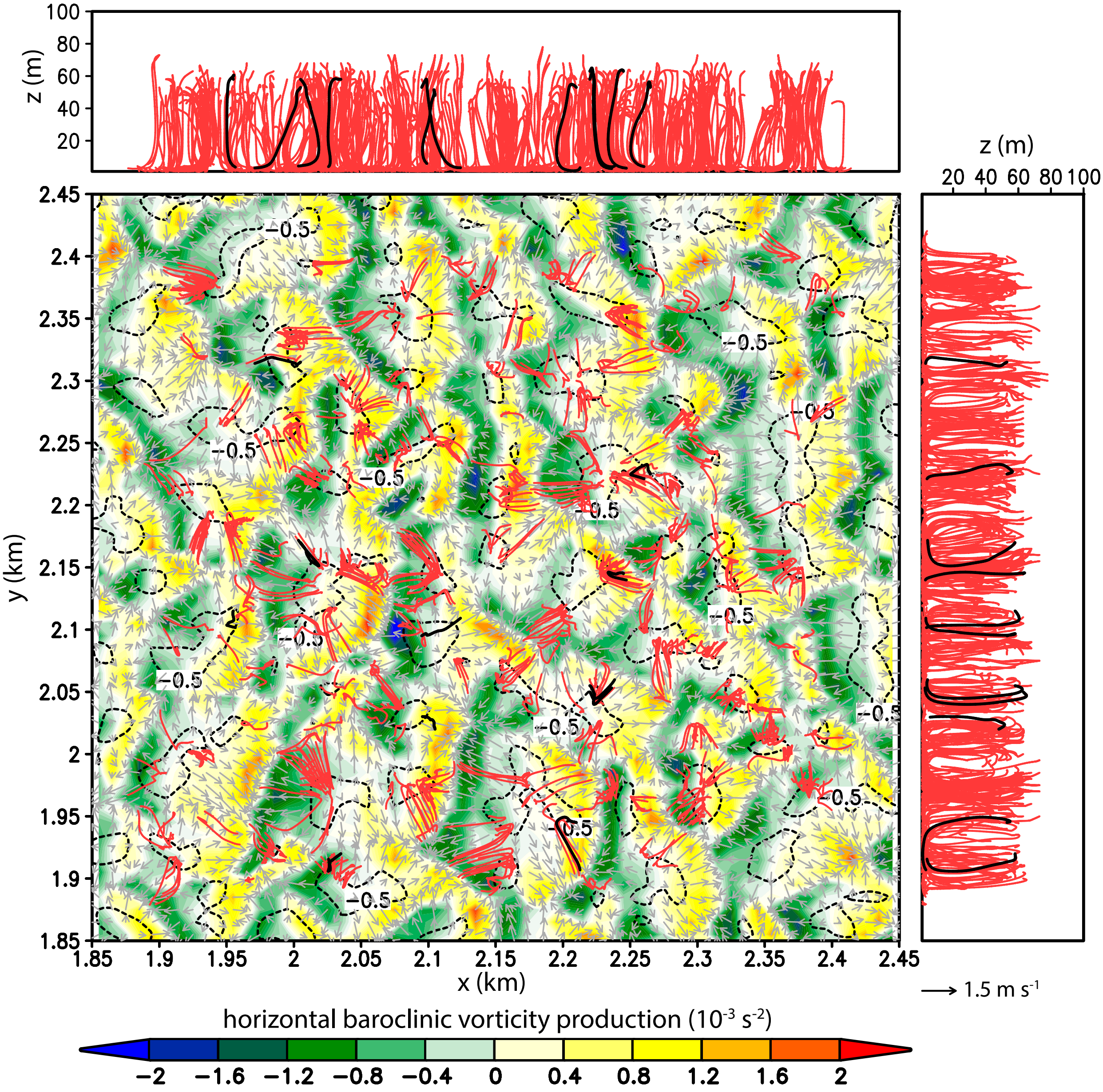

FIG. 3. Trajectories ($n = 584$) that acquire weak near-surface vertical vorticity are shown as red line segments. The plan view also shows horizontal velocity vectors at the lowest model level (2.5 m AGL), as well as the magnitude of horizontal baroclinic vorticity production (shaded) and downdraft speed at 12.5 m AGL (contoured, $w = -0.5$ m s^{-1}) at 600 s. The black line segments represent the 11 trajectories analyzed in detail. In this plot, the baroclinic vorticity production strength is approximated as $|\nabla_h B|$, where B is the buoyancy.

acquiring their horizontal vorticity (Fig. 4b). This baroclinically produced vorticity is associated with the convective circulations that make up the CBL. Horizontal stretching of the baroclinically produced vorticity occurs as the horizontal flow diverges and accelerated away from the downdraft center. Turbulent mixing and numerical diffusion contribute slightly negatively close to the ground.

The vertical vorticity budgets are shown in Fig. 4b. Aside from relatively small contributions from SGS mixing and implicit diffusion, positive vertical vorticity arises from upward tilting of the baroclinically produced horizontal vorticity while the parcels are descending. The effect of the stretching term is negative because of horizontal divergence at the base of the downdraft. This vertical vorticity acquisition is visualized in Fig. 5, which shows the vorticity vectors along the average trajectory in the (x, z) plane. The vorticity vectors are initially negligibly small in magnitude and subsequently attain a nonzero horizontal component due to baroclinic production. As the trajectory approaches the ground, the vorticity is tilted upward (using all 584 parcels to calculate the average vorticity evolution reveals the same general picture of upward tilting during descent).

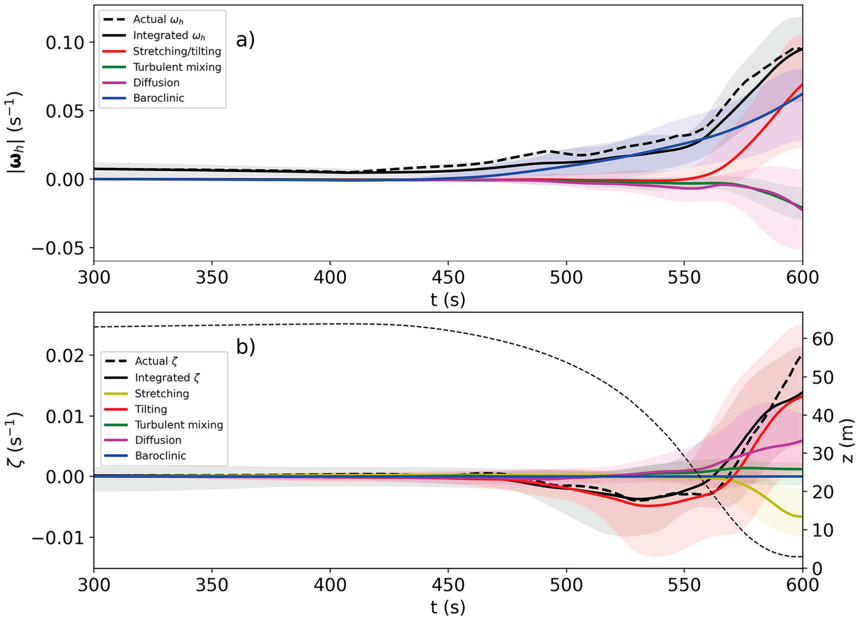

FIG. 4. (a) Integrated budgets of the horizontal vorticity magnitude of the average trajectory ($n = 11$). The shaded areas show the 10th–90th percentiles of the integrals. (b) As in (a), but for the vertical vorticity component. The average parcel height is shown as the black dashed line (the heights are shown on the axis on the right side of the panel).

Why is the horizontal baroclinic vorticity reoriented in downdrafts? First, consider the tilting term T of the vertical vorticity equation, which may be written as (e.g., Parker and Dahl 2015)

$$T = \boldsymbol{\omega}_h^{\mathrm{shr}} \cdot \nabla_h w, \tag{3}$$

where $\boldsymbol{\omega}_h^{\mathrm{shr}} = \mathbf{k} \times \partial \mathbf{v}_h / \partial z$ is the horizontal vorticity associated with the vertical variation of the horizontal wind, which in this case is tied to the "outflow" beneath the descending branch of the convective cells. It is clear that the orientation of the horizontal vorticity is influenced by the direction of the outflow (via $\partial \mathbf{v}_h / \partial z$). Also, Eq. (3) shows that the horizontal vortex lines can only be reoriented if they intersect w contours.

To demonstrate the general principle of how the horizontal geometry of downdrafts affects vertical-vorticity production, two separate, idealized downdraft simulations were run also using the CM1 model, but in a different configuration than the CBL simulation. The simulations feature an artificial heat sink, which triggers and maintains a downdraft. The model settings are essentially the same as in Parker and Dahl (2015) and Fischer and Dahl (2020) and are summarized in the appendix. For these simulations, a horizontal grid spacing of 50 m was used. The heat sink had a circular horizontal footprint in one simulation and an elliptic footprint in the other.

In the simulation with the circular footprint, surface outflow spreads out radially, implying that the baroclinically produced vortex lines likewise are circles, and consequently they do not intersect the updraft contours as shown in Fig. 6a. As a result, the vertical vorticity at the surface remains practically zero, as seen in Fig. 6b. The reason that the outflow spreads out in an axisymmetric manner is that the region of high pressure, which drives the horizontal outflow, likewise is circular at low levels (red contours in Fig. 6c). This behavior is ultimately tied to the fact that the Laplacian of the pressure field is approximately determined by velocity and buoyancy gradients (e.g., Rotunno and Klemp 1982). In the Boussinesq limit, this may be written as

$$-\frac{1}{\rho_0}\nabla^2 p' = \left[\left(\frac{\partial u}{\partial x}\right)^2 + \left(\frac{\partial v}{\partial y}\right)^2 + \left(\frac{\partial w}{\partial z}\right)^2\right] + 2\left(\frac{\partial u}{\partial y}\frac{\partial v}{\partial x} + \frac{\partial u}{\partial z}\frac{\partial w}{\partial x} + \frac{\partial v}{\partial z}\frac{\partial w}{\partial y}\right) - \frac{\partial B}{\partial z}, \tag{4}$$

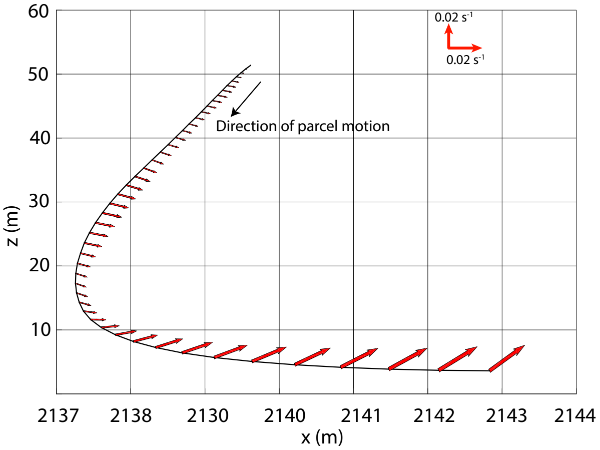

FIG. 5. Projection of the 3D average trajectory ($n = 11$) and its vorticity vectors onto the (x, z) plane.

where ρ_0 is the base-state density and p' is the perturbation pressure [see, e.g., Markowski and Richardson (2010, p. 27) for a derivation and interpretation of this equation]. The terms in the first square bracket are referred to as the fluid-extension (FE) terms, and the second bracket contains the shear terms; the last term describes buoyancy (B) forcing. This equation may be used to attribute the pressure field to flow features (e.g., a stagnation point is associated with pressure maximum). In the downdraft simulations, the largest forcing comes from the fluid-extension terms, which are also shown in Fig. 6c for the circular downdraft geometry. Indeed, the perturbation pressure forcing is positive (implying positive perturbation pressure), and it is axisymmetric, thus driving radial outflow (Fig. 6c).

If the horizontal footprint of the downdraft is elliptic, the symmetry is broken and $\boldsymbol{\omega}_h^{\mathrm{shr}}$ does intersect the w contours as depicted in Fig. 7a. The tilting term exhibits a quadrupole pattern, resulting in a cloverleaf-like distribution of vertical vorticity at the lowest model level (Fig. 7b).[3] As shown in Fig. 7c, the fluid-extension terms are maximized beneath the downdraft, and they exhibit nearly the same ellipticity as the downdraft contours. The pressure field itself, however, is more circular than the downdraft contours because the solution of a Poisson equation tends to be more "spread out" than the forcing (e.g., Shapiro and Kanak 2002). Since the outflow is driven by the horizontal perturbation pressure gradient, $\mathbf{v}_h$ is nonorthogonal to the w contours, and $\boldsymbol{\omega}_h^{\mathrm{shr}}$ is nonparallel to the w contours. The result is upward/downward tilting of the baroclinically produced horizontal vorticity in descending air. Shapiro and Kanak (2002) discuss a similar scenario in the context of an ellipsoidal thermal, which results in a quadrupole-like distribution of vertical vorticity within the thermal [in their case, the perturbation pressure field is forced by the buoyancy term in Eq. (4), however].

Indeed, 1270 s into the present CBL simulation, a downdraft loosely featuring a cloverleaf-like vertical-vorticity field is present as shown in Fig. 8 (most downdrafts produce less organized vertical vorticity patterns because they exhibit seemingly arbitrary nonaxisymmetric geometries).

The cellular vertical-vorticity pattern at the lowest model level gradually widens and intensifies as the CBL deepens [as also found by Kanak et al. (2000)]. However, the vertical vorticity at the bottom of the CBL is still maintained primarily by

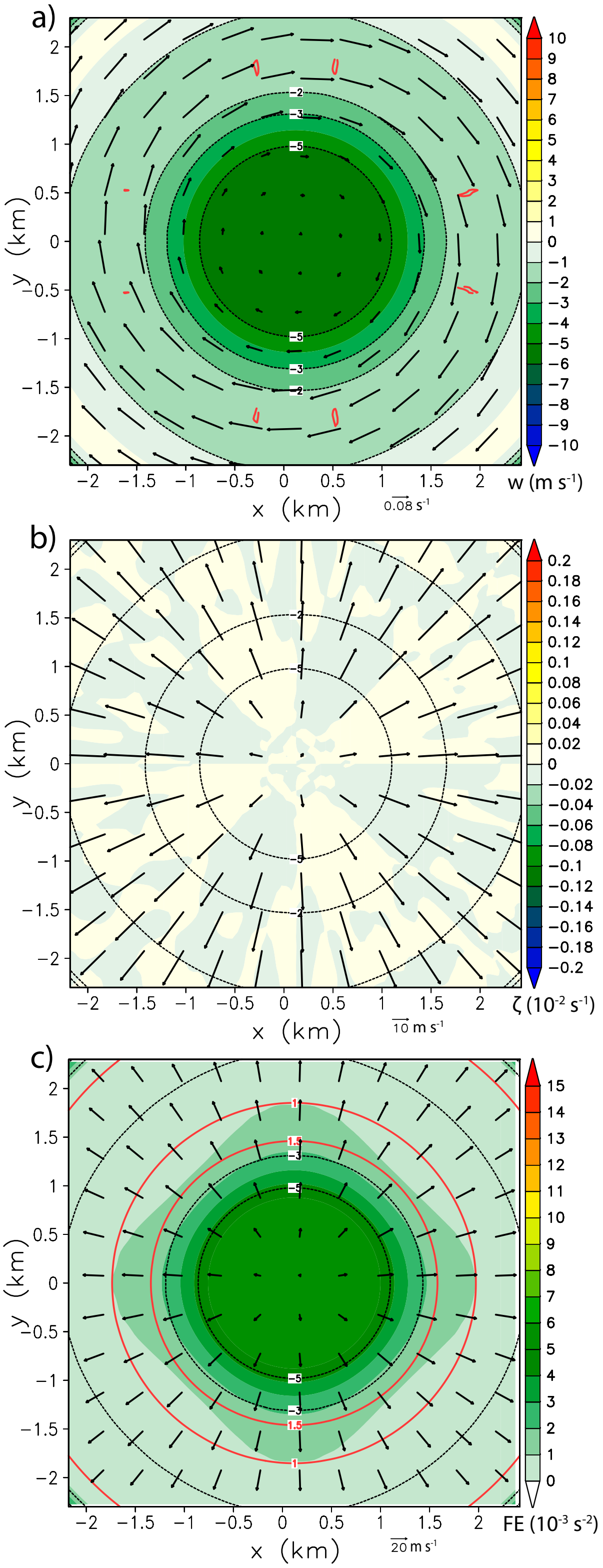

FIG. 6. (a) Vertical velocity [shaded and contoured, (−5, −3, −2, −1) s^{-1}], horizontal vorticity $\boldsymbol{\omega}_h^{\mathrm{shr}}$ (arrows), and the tilting term of the vertical vorticity equation (contoured in red, −2, −1, 1, 2 × 10^{-4} s^{-2}) at 142 m AGL. The tilting term is theoretically zero

←

but attains small values due to numerical noise. (b) Vertical velocity at 142 m AGL [contoured, (−5, −2, −1, 1, 2, 5) m s^{-1}] and 2.5 m AGL wind vectors (arrows) as well as 2.5 m AGL vertical vorticity (shaded). (c) FE terms (shaded), perturbation pressure [red contours, (0.5, 1.0, 1.5) hPa] at 2.5 m AGL, wind vectors at 2.5 m AGL, and vertical velocity at 142 m AGL [black contours, (−5, −2, −1, 1, 2, 5) m s^{-1}]. The time is 360 s for all panels.

---

[3] The noise at the leading edge of the outflow is in part related to dispersion errors and in part to initial near-surface vorticity production that seems to be related to the semi-slip lower boundary condition.

the same baroclinic mechanism just described. Indeed, Fig. 9 shows that the horizontal vorticity vectors are mostly parallel to the potential-temperature contours at 1420 s, implying that the vorticity is predominantly of baroclinic origin. The tilting term is also shown in Fig. 9, but to reduce clutter, only the positive values are considered; also, the tilting term is only plotted where it coincides with downdraft to highlight regions where vertical vorticity arises in descending air (black contours in Fig. 9). The red contours show the resulting positive vertical vorticity, which tends to be located close to the regions of positive tilting, though there is some offset because vertical vorticity is maximized where the most vertical stretching has subsequently been accumulated, which is in regions of horizontal convergence at the periphery of the downdraft cells. Negative vertical vorticity contours are suppressed in Fig. 9 for better visibility, but the downdraft mechanism produces positive and negative vertical vorticity with the average vertical vorticity in the domain being practically zero.

To summarize, it is the nonaxisymmetric horizontal footprint of the downdraft cells that allows for the baroclinically produced horizontal vorticity to be tilted into the vertical within the downdrafts. In this simulation, this mechanism is the origin of vertical vorticity at the lowest model level.

As the CBL grows, an interesting aspect becomes evident: After an initial increase, the average vertical vorticity magnitude at the lowest model level decreases in time (Fig. 10b), while the maximum increases (Fig. 10c). The reason is that the regions of vertical vorticity accumulate beneath the horizontally convergent updraft regions of the convective cells. As the diameter of the cells increases, there are larger "voids" of vertical vorticity while the intensity of the vorticity increases.

c. *Vortex formation*

The presence of vertical vorticity at the lowest model level does not imply the presence of vortices (e.g., Jeong and Hussain 1995). The reason is that aside from vorticity, there usually is also nonzero straining motion present in the flow. If, e.g., there is deformation and vorticity,[4] and each has the same magnitude, the result is simply a sheared, unidirectional flow within the patch of vorticity (Fig. 11a; see also Batchelor 2002, p. 83). Only if the vorticity is much stronger than the straining motion, the flow exhibits a spinning motion and a vortex is present (Fig. 11b). In the ideal case of pure, solid-body-like rotation, the straining motion is zero.

The dominance of vorticity over straining motion, i.e., whether or not a vortex is present, may be diagnosed using the Okubo–Weiss number OW (Okubo 1970; Weiss 1991), which is given by the difference between the squared vorticity and deformation magnitudes,

$$\mathrm{OW} = \zeta^2 - D_1^2 - D_2^2, \qquad (5)$$

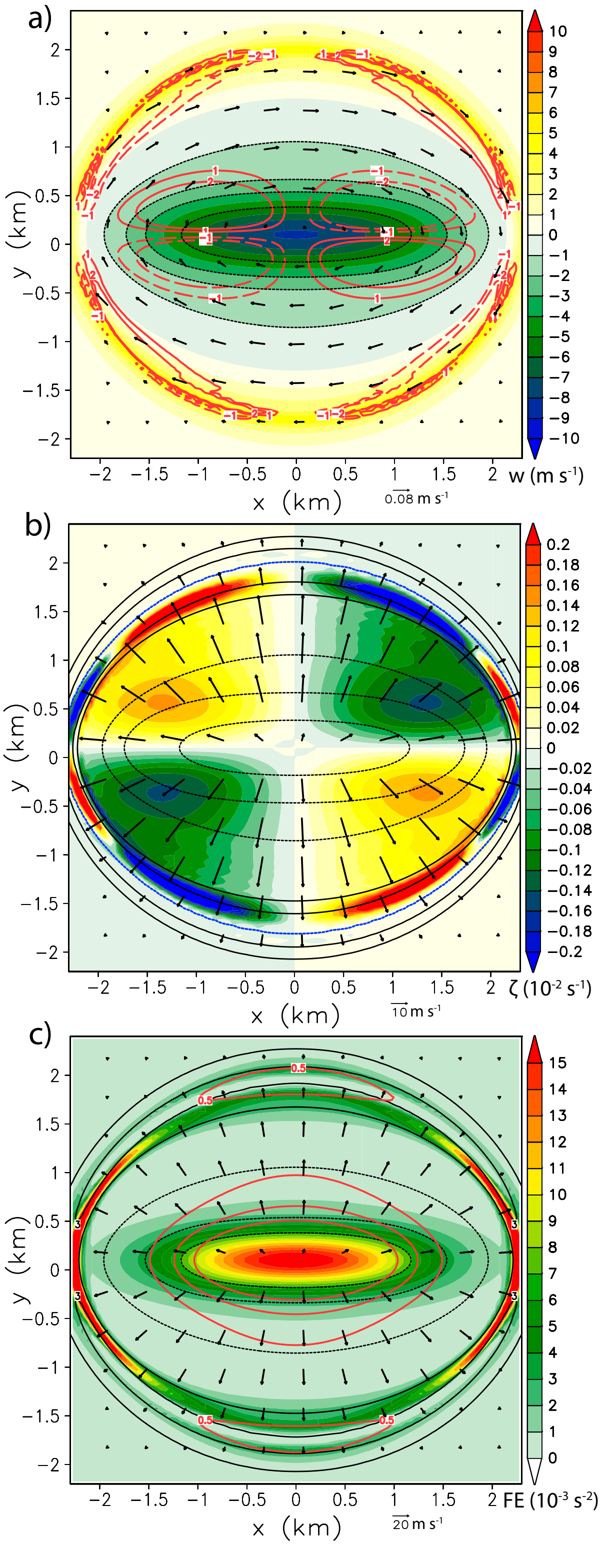

FIG. 7. (a) Vertical velocity [shaded and contoured, (−5, −3, −2, −1) × m s^{-1}], horizontal vorticity $\boldsymbol{\omega}_h^{\mathrm{shr}}$ (arrows), and the tilting term of the vertical vorticity equation (contoured in red, −2, −1, 1, 2 × 10^{-4} s^{-2}) at 142 m AGL. (b) Vertical velocity at 142 m AGL [contoured, (−5, −2, −1, 1, 2, 5) m s^{-1}] and 2.5 m AGL wind

---

[4] Unless specified otherwise, hereafter, vorticity refers to vertical vorticity and deformation refers to horizontal deformation.

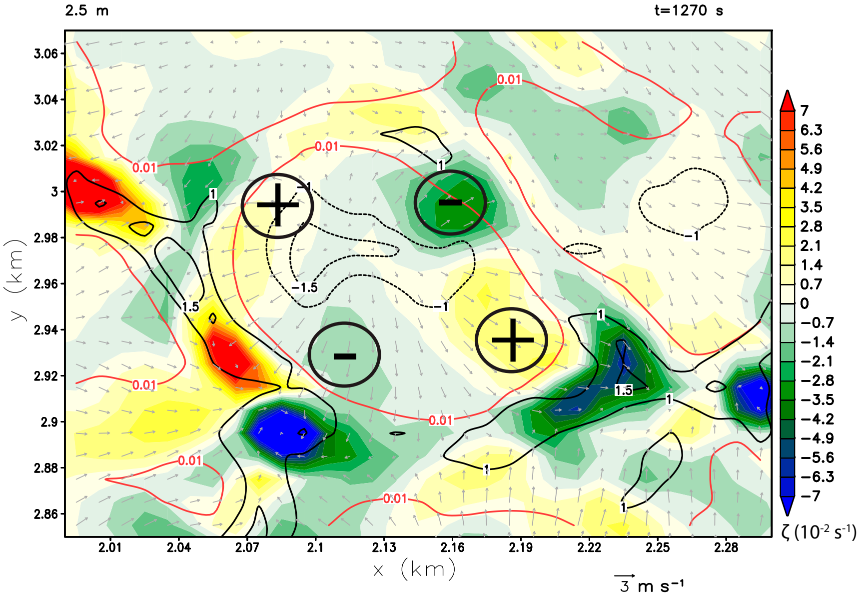

FIG. 8. Vertical vorticity (shaded; plus and minus signs show the signs of vertical vorticity extrema produced by the downdraft) at the lowest model level (2.5 m AGL) at 1270 s. Also shown is the vertical velocity at 22.5 m AGL (black contours; m s^{-1}) and horizontal convergence at 2.5 m AGL (red contour; 0.01 s^{-1}).

where $D_1 = \partial v/\partial x + \partial u/\partial y$ and $D_2 = \partial u/\partial x - \partial v/\partial y$ are the shearing and stretching deformation, respectively. If OW $\gg 0$, the flow is rotation-dominated, and closed streamlines and a low pressure center are present (see also Wu et al. 2006, p. 310). For the vortex patches embedded in deformation flow (Fig. 11), it is seen that indeed the OW number is positive in the case where rotation is visible (Fig. 11b).

In the present simulation, the straining motion is associated with the convective cells. Deformation, like horizontal convergence, is maximized beneath the low-level updraft regions, serving as conduits where the vortex patches are collected and along which the vortex patches propagate (Fig. 12). The maximum deformation magnitude at the lowest model level increases as the CBL grows (Fig. 10d). Despite this increase, Fig. 10e shows that the maximum OW still grows as the simulation progresses, implying that vorticity progressively dominates over deformation and that vortex patches increasingly become associated with vortices (e.g., closed streamlines and low pressure centers). Why does the vorticity become dominant relative to the deformation?

The initial vortex patches are small in size and weak in magnitude and seem to exhibit behavior similar to that shown in Fig. 11a, which is a linear superposition of the deformation and rotation parts with no closed streamline patterns. Hence, their small OW numbers are as seen in Fig. 13a. A possible explanation for the subsequent increase in OW is that horizontal convergence strongly affects the vertical vorticity due to conservation of angular momentum, while the deformation magnitude appears not to be affected as much by horizontal convergence. The result is that vorticity increases beyond the deformation magnitude.

Moreover, aside from an increase of vorticity, the deformation magnitude tends to decrease within the developing vortex cores (Fig. 14). The reason for the decrease of the deformation is not obvious but may be related to mergers of individually weak, like-signed vortex patches, also visible in Fig. 14. These mergers are mostly a stochastic process, depending on the supply of like-signed vortex patches from the downdraft regions. Following these mergers, the resulting vortex patch increases in size, and at that point, there appears to be a significant amount of interaction between the deformation and rotation parts of the flow, and the deformation decreases in the vortex core (and it increases outside the vortex core, which may contribute to the increase of deformation in Fig. 10d). A similar behavior was observed in the idealized 2D simulations by Dahl (2020), who showed that during vortex formation, while the vorticity remained constant, the ratio between vorticity and deformation increased (implying a decrease in deformation in the developing vortex core). It seems that both of these effects, the increase in vorticity via stretching and the decrease in deformation within the vortex patches, lead to an increase in the OW number and hence vortex formation.

d. Vorticity dynamics of a maturing vortex

Although the dynamics of the mature vortices are not the focus of this study due to their somewhat poor representation

---

←
vectors (arrows) as well as 2.5 m AGL vertical vorticity (shaded). (c) FE terms (shaded), perturbation pressure [red contours, (0.5, 1.0, 1.5) hPa] at 2.5 m AGL, wind vectors at 2.5 m AGL, and vertical velocity at 142 m AGL [black contours, (−5, −2, −1, 1, 2, 5) m s^{-1}]. The time is 360 s for all panels.

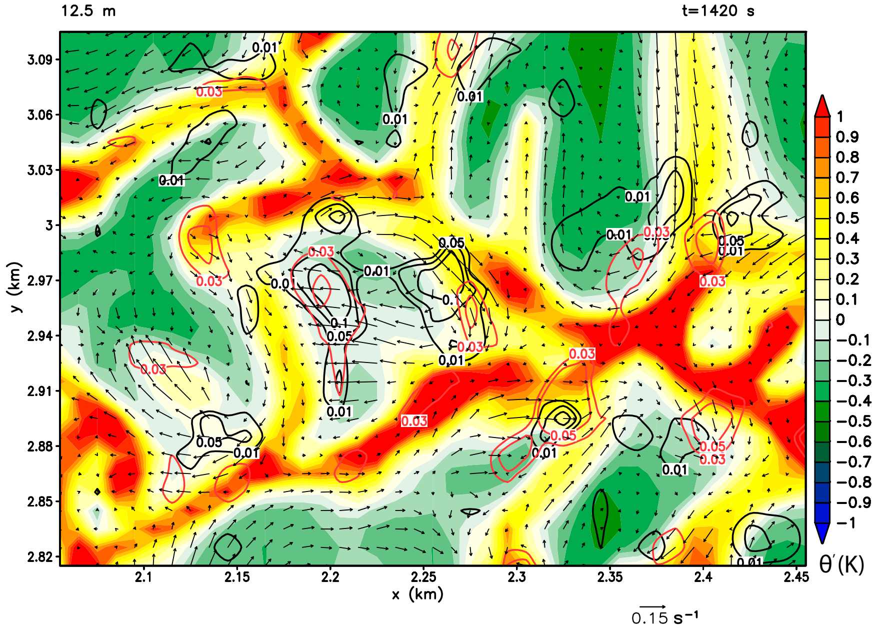

FIG. 9. Horizontal vorticity vectors (arrows), potential temperature perturbations (shaded), and tilting term [black contours, $(0.01, 0.05, 0.1) \times 10^{-2}$ s^{-2}] shown only where $w < 0$, at 12.5 m AGL and 1420 s. Vertical positive vorticity at 12.5 m AGL (s^{-1}) is shown in red contours.

given the relatively coarse resolution of the simulation, a few insights into the structure and dynamics of these vortices may still be gleaned.

Notably, as circular streamlines are attained, the flow interacts with the lower boundary, and the structure of the vortices in the present simulation is broadly consistent with seminal early work that has focused on the interaction of a vortex with the lower boundary, e.g., Barcilon (1967), Burggraf et al. (1971), and Rotunno (1980). That work has more recently been reviewed and expanded upon by Rotunno (2013, 2014). The main idea is that a vortex boundary layer develops, in which, due to the frictional retardation of the near-ground azimuthal flow, radial vorticity arises (i.e., the horizontal near-ground vorticity vectors point toward the vortex axis in a cyclonic vortex). In addition, the air in the vortex boundary layer accelerates toward the vortex center because of the imbalance between the pressure-gradient force and the centrifugal force in that layer (e.g., Rotunno 2013). As a consequence, the boundary layer air converges toward the axis of rotation where this air is forced to rise, thereby abruptly tilting the radial vorticity into the vertical in the vortex center. The result is a swirling upward-directed jet, a configuration referred to as an endwall vortex because the jet consists of the endwall boundary layer air of the parent vortex (Rotunno 2013). As shown in Fig. 15a, there is indeed radial vorticity at the base of the vortices shown. Now, because the 3D vorticity vector field is solenoidal, i.e., $\nabla \cdot \boldsymbol{\omega} = 0$, it follows that

$$\nabla_h \cdot \boldsymbol{\omega}_h = -\frac{\partial \zeta}{\partial z}. \tag{6}$$

That is, in a region where the horizontal vortex lines converge near the surface, they must bend upward, as supported by Fig. 15b (The vorticity vectors point away from the vortex center in anticyclonic vortices, as seen in Fig. 15a). These results are consistent with the analysis by Simpson and Glezer (2016), who likewise found that it was the near-ground horizontal vorticity associated with surface drag that is tilted upward at the base of their modeled vortex. In the present simulation, the radial inflow into the vortex is comparatively weak, probably because the vortex boundary layer is poorly resolved. However, the tilting term is indeed positive at the base of the vortex (but exhibits a wavenumber $m = 2$ asymmetry), as seen in Fig. 16.

This brief analysis is consistent with the notion that, as the vortex matures, it is mainly radial vorticity due to surface drag that feeds into the vortex base—in contrast to the early stages, where the main vorticity source is baroclinic production. Similar dynamics were recently identified in idealized simulations of tornado-like vortices (Fischer and Dahl 2022) and are also implied by the conceptual model of Raasch and Franke (2011; their Fig. 15).

4. Discussion

a. Relation to previous vorticity analyses

The results presented here are consistent with previous studies. Importantly, horizontal baroclinic vorticity production and subsequent tilting has long been considered a viable source of vertical vorticity (e.g., Carroll and Ryan 1970; Kanak et al. 2000; Fiedler and Kanak 2001; Renno et al. 2004; Ito et al. 2010, among others). A new aspect in the present study is the identification of the baroclinic downdraft mechanism that leads to vertical vorticity at the bottom of the CBL,

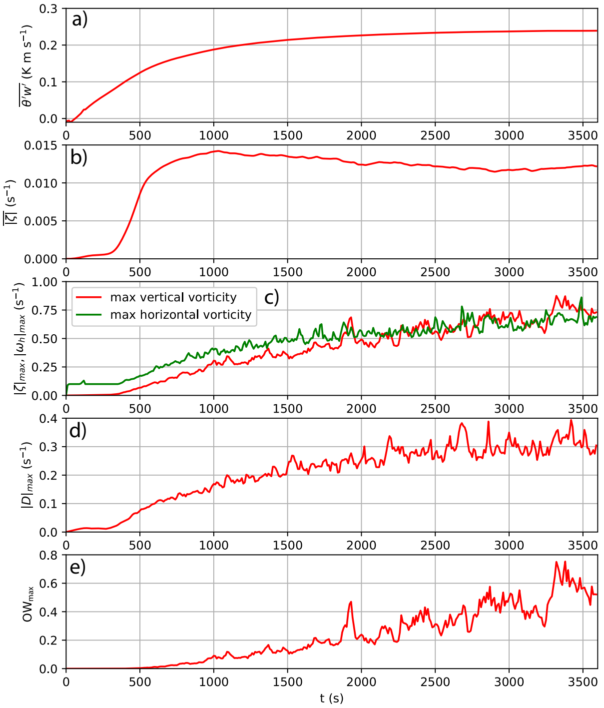

FIG. 10. Time series of (a) sensible heat flux, $\overline{\theta' w'}$, (b) average vertical vorticity magnitude at the lowest model level, (c) maximum vertical vorticity magnitude at the lowest model level (red line) and domain-wide maximum horizontal vorticity (green line), (d) maximum deformation magnitude at the lowest model level, and (e) maximum Okubo–Weiss number at the lowest model level.

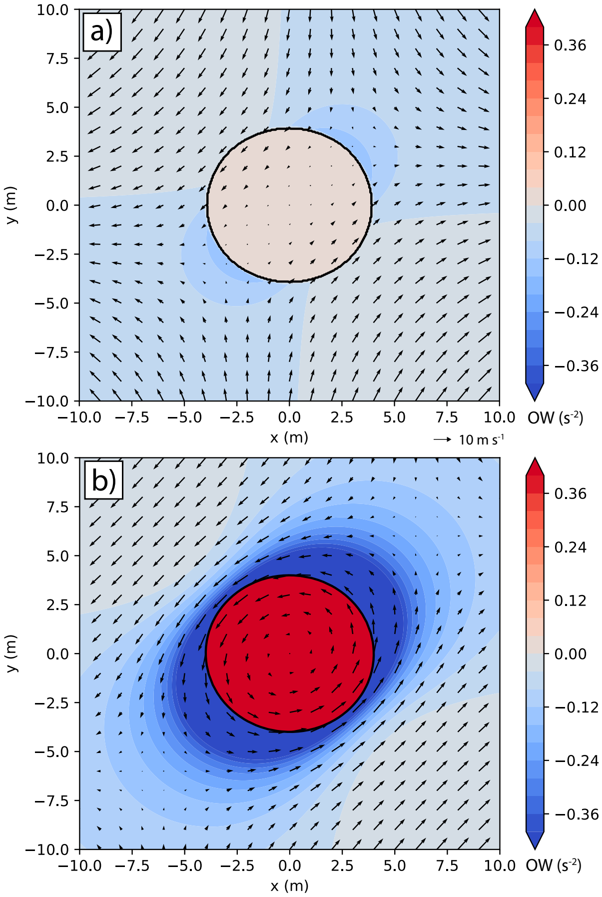

FIG. 11. (a),(b) Example of the linear superposition of a flow field characterized by stretching deformation, and the flow associated with a circular uniform vortex patch (i.e., a Rankine vortex profile). In (a), the deformation strength is the same as the rotation strength (0.2 s^{-1}), and the result is a sheared, rectilinear flow in the vortex patch (black circle). In (b), the rotation magnitude is 5 times that of the deformation, and a vortex is present.

which is the ultimate origin of DDLVs in the present simulation. Moreover, studies considering fully developed vortices have consistently found that tilting and stretching is large at the vortex base (e.g., Ohno and Takemi 2010; Raasch and Franke 2011; Ito et al. 2010; Simpson and Glezer 2016). These findings are consistent with the abrupt upward tilting of horizontal vorticity generated at the lower boundary found in the present analysis after the vortex has formed.

When considering the origin of the vortex, the vorticity prior to its development is most relevant; once a fully developed vortex is present, its interaction with the lower boundary typically reveals large tilting and stretching of the vorticity present in the vortex boundary layer. While this aspect is relevant for the maintenance (and perhaps, decay) of the vortex, the vorticity budgets at that point usually no longer reveal why the vortex formed in the first place.

b. *Potential additional vorticity contributions*

One possible origin of vorticity was excluded from this study by using a resting initial state. Real-world CBLs are usually sheared given nonzero horizontal background flow. In sheared CBLs, the horizontal vorticity associated with the background flow may be tilted into the vertical and potentially contribute to weak vertical vorticity. However, it seems that fundamentally the background wind shear is not needed because boundary layer vortices also form without its presence. Indeed, too strong a background flow seems to be detrimental to dust-devil formation (e.g., Ito et al. 2010), probably because the superadiabatic surface layer is weakened due to turbulence in strong-wind conditions (Rafkin et al. 2016). Perhaps the elongated downdraft geometry in sheared flows also affects the surface vertical vorticity production (horizontal rolls may be less efficient in delivering vertical vorticity at the ground).

c. *Possible alternative view on rapid vortex spin-up*

Visually, it often appears that a dust devil is the result of a particularly buoyant thermal that suddenly rises, thereby rapidly concentrating the available surface vertical vorticity via vertical stretching. However, based on the argument in the previous section, it also seems possible that the rapid vortex intensification may be dominated by the development of the radial inflow associated with the secondary circulation in the

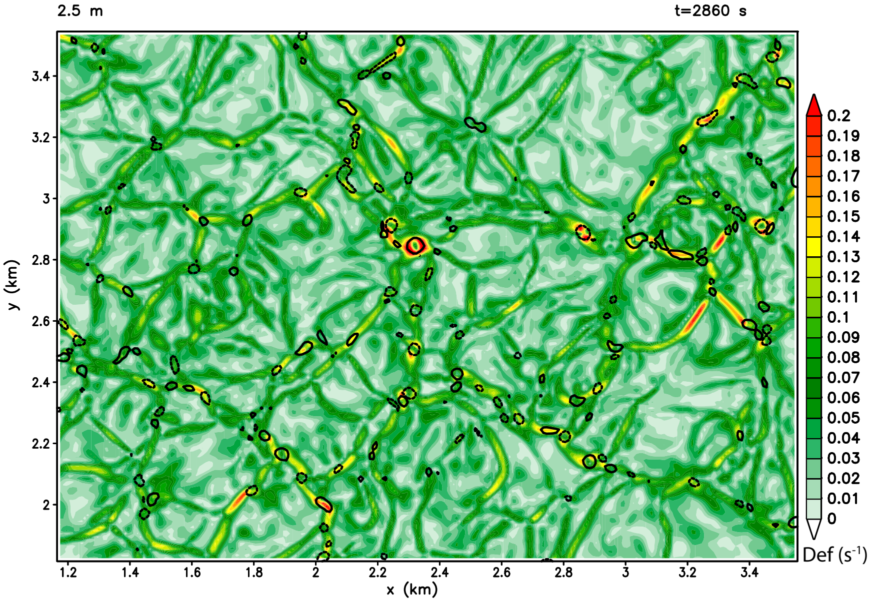

FIG. 12. Deformation magnitude (Def = $\sqrt{D_1^2 + D_2^2}$; shaded), and vertical vorticity at the lowest model level [contoured, $\zeta = (-0.05, 0.05)\ \mathrm{s}^{-1}$] at 2860 s.

vortex boundary layer. In this case, one might likewise observe a sudden onset of rotation and near-surface upward motion. As this intensification does not require buoyancy forces (e.g., Rotunno 2014), the upward acceleration would mainly be driven by the dynamic vertical perturbation pressure gradient force.

d. *Requirement for vertical-vorticity production at the downdraft base*

The present analysis suggests that negatively buoyant downdrafts tend to produce surface vertical vorticity as long as their horizontal geometry is noncircular. Previous analyses identified nonzero downdraft-relative flow as requirement for vertical-vorticity production in downdrafts (e.g., Davies-Jones 2002; Straka et al. 2007; Parker and Dahl 2015). In Parker and Dahl's (2015) analysis, the through-flow was needed because the heat sink was circular, so the only way of creating nonaxisymmetric downdrafts was the ambient wind. This condition is not necessary, however, as shown herein. That is, even without background flow, the downdraft structures tend to be nonaxisymmetric. This has important ramifications for precipitating deep convection: Whenever the downdraft footprint is noncircular (i.e., in practically all cases), one should expect regions of nonzero vertical vorticity within the storm's downdraft. While this vertical vorticity in most instances cannot easily be concentrated, it suggests that practically all precipitating convective clouds likely produce at least some weak vertical vorticity within their outflow.

e. *Parallels to the vorticity dynamics of supercell tornadoes*

The chain of events presented here that lead to the formation of dust-devil-like boundary layer vortices in many respects resembles the mechanisms by which tornadoes form in supercells in the absence of preexisting vertical vorticity (e.g., Fischer et al. 2024). In supercells, the negatively buoyant main downdraft northeast of the mesocyclone produces horizontal vorticity baroclinically at its periphery (e.g., Rotunno and Klemp 1985; Markowski and Richardson 2014; Dahl et al. 2014; Parker and Dahl 2015). It is this initially horizontal vorticity that is tilted into the vertical while the air is descending, resulting in regions of vertical vorticity in the storm's outflow (e.g., Davies-Jones and Brooks 1993; Markowski and Richardson 2014; Fischer and Dahl 2020). This baroclinic downdraft mechanism, at a smaller scale, is also responsible for the vertical vorticity at the bottom of the CBL. In supercells, this vorticity subsequently intensifies due to horizontal convergence along the leading edge of, as well as along internal boundaries within, the storm's outflow. As in the CBL, the resulting vertical vorticity maxima in supercells organize and merge (Dahl 2020; Parker 2023), eventually leading to pressure deficits and circular streamlines, setting the stage for vortex intensification as the secondary circulation in the vortex boundary layer develops (e.g., Fischer et al. 2024). From a pure vorticity dynamics perspective, tornado formation in a supercell and dust-devil formation thus seem rather similar.

5. Conclusions

An evolving dry convective boundary layer in an initially resting atmosphere was simulated using the CM1 model. In the simulation, weak vertical vorticity develops at the surface as soon as convective mixing sets in. The present analysis reveals that

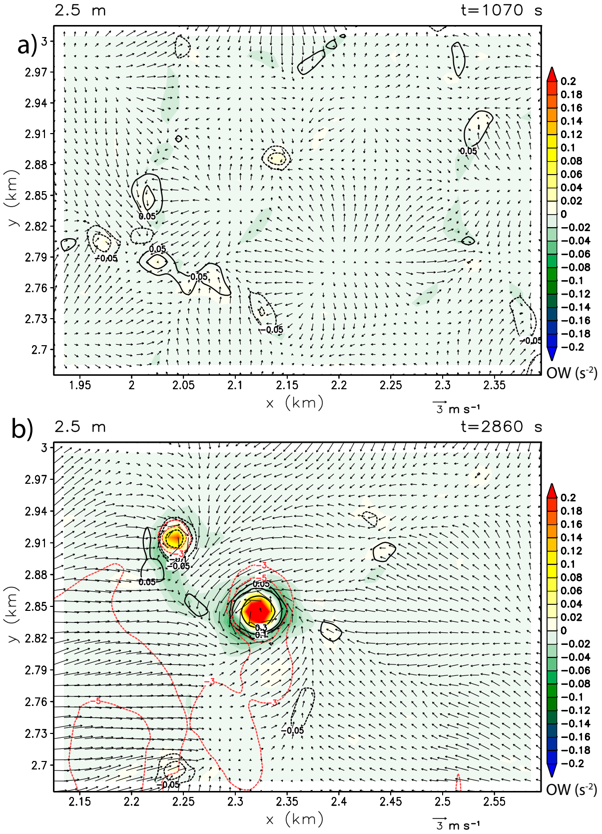

FIG. 13. Okubo–Weiss number (shaded), vertical vorticity [contoured, $\zeta = (-0.3, -0.1, -0.05, 0.05, 0.1, 0.3)\ \mathrm{s}^{-1}$], and horizontal wind vectors at the lowest model level, at (a) 1070 and (b) 2860 s.

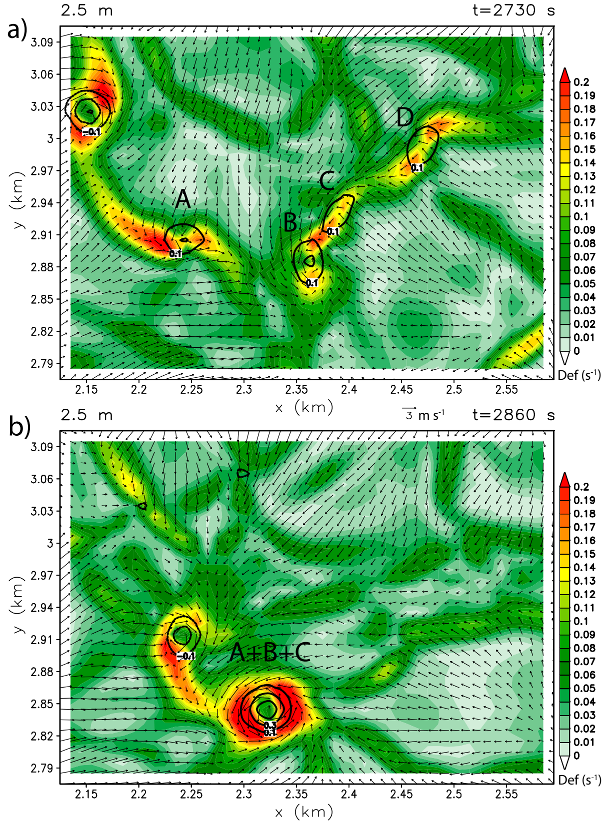

FIG. 14. Deformation magnitude (shaded), horizontal wind vectors, and vertical vorticity [contoured, $\zeta = (-0.5, -0.3, -0.1, 0.1, 0.3, 0.5)\ \mathrm{s}^{-1}$] at the lowest model level: (a) 2730 and (b) 2850 s. The labels A–D refer to individual cyclonic vortex patches.

- Vertical vorticity at the ground results from horizontal baroclinic vorticity production at the periphery of the downdraft cells; this vorticity is tilted into the vertical in sinking air due to the nonaxisymmetry of the downdraft regions, and subsequently swept beneath updraft regions, where the vertical vorticity is amplified due to horizontal convergence. This basic mechanism has previously been identified in simulated supercell thunderstorms.
- The only requirement for a negatively buoyant downdraft to produce surface vertical vorticity is that it has a noncircular horizontal footprint; previous work has indicated that it is horizontal flow through the downdraft that facilitates surface vertical vorticity development. The present results suggest that the ultimate cause is the resulting noncircular geometry of the downdraft.
- Initially, the resulting vertical surface vorticity is overwhelmed by deformation, such that barely any rotation is present. Vortices develop later in the simulation as vertical stretching amplifies the vertical vorticity and as deformation decreases in the developing vortex core, often following mergers of like-signed vortex patches.
- A brief analysis of a mature DDLV suggests that its basic dynamics are influenced by the lower boundary. Radial vorticity due to surface drag is present at the base of the vortex, and the associated vortex lines bend upward into the vortex, consistent with previous analyses of idealized columnar vortices.

Acknowledgments. The author appreciates the assistance of Dr. Christian Boyer in setting up the CBL simulation. Helpful discussions with Drs. Paul Markowski, Sandip Pal, Matt Parker, Rich Rotunno, and Alan Shapiro are gratefully acknowledged. Dr. George Bryan generously maintains the CM1 model, without which this research would not have been possible. Three anonymous reviewers provided valuable comments that led to additional analysis and improved the clarity of the presentation. Figures were created using the Python Matplotlib package as well as the Grid Analysis and Display System (GrADS). Partial financial support for this study was provided by NSF under Grant AGS-2152537.

Data availability statement. The namelist settings of the CM1 model as well as the source code are available from the author's GitHub repository at https://github.com/joda80/dust_devils.

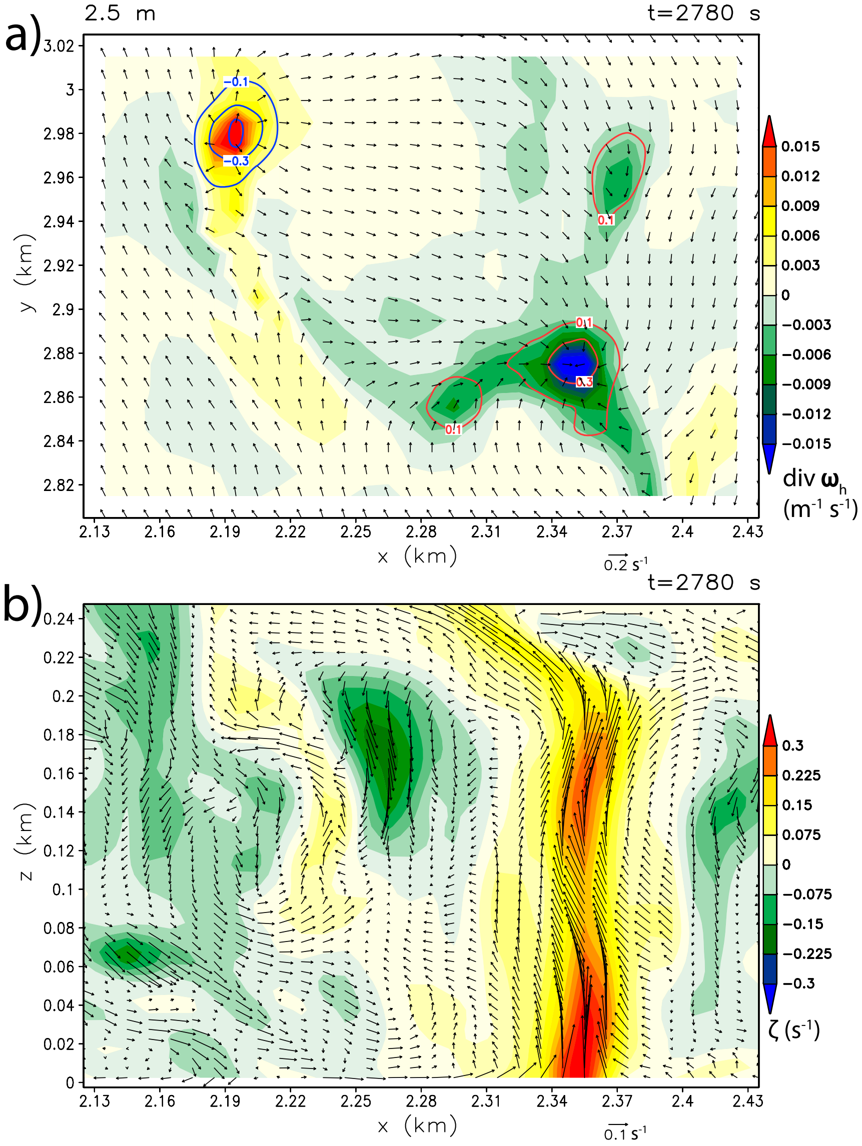

FIG. 15. (a) Horizontal divergence of the horizontal vorticity vectors (shaded; $\mathrm{m}^{-1}\ \mathrm{s}^{-1}$), horizontal vorticity vectors (arrows), and vertical vorticity [red contours, $(-0.3, -0.1, 0.1, 0.3) \times \mathrm{s}^{-1}$] at $z = 2.5$ m AGL and 2780 s. (b) Vertical cross section of vertical vorticity (shaded) and vorticity vectors in the (x, z) plane (arrows) at $y = 2885$ m.

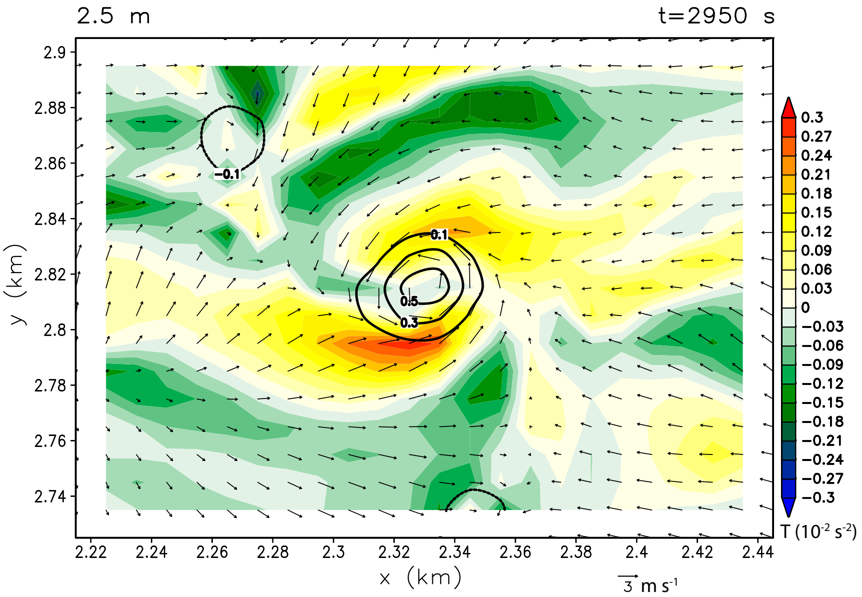

FIG. 16. Tilting term of the vertical vorticity equation (shaded), horizontal wind vectors, and vertical vorticity [contoured, $\zeta = (-0.5, -0.3, -0.1, 0.1, 0.3, 0.5)$ s^{-1}] at the lowest model level at 2950 s.

APPENDIX

Model Settings of the Idealized-Downdraft Simulations

The settings of the idealized downdraft simulations are shown in Table A1. The heat sink was ramped up linearly over a period of 300 s. Since the interest was focused on the qualitative behavior of the downdrafts, a shallow domain of 3.5-km depth was deemed sufficient for the intended purpose.

TABLE A1. Model settings of the idealized downdraft simulations. The settings pertain to the simulation with a circular horizontal footprint of the downdraft as well as the simulation with an elliptic horizontal footprint of the downdraft. The simulations only vary in the horizontal dimensions of the heat sink.

Model setting	Circular	Elliptic
nx	360	360
ny	360	360
nz	70	70
dx	50 m	50 m
dy	50 m	50 m
dz	10 m, increasing to 90 m at 3500 m AGL	10 m, increasing to 90 m at 3500 m AGL
Domain size	$18 \times 18 \times 3.5$ km^3	$18 \times 18 \times 3.5$ km^3
Heat-sink strength	0.1 K s^{-1}	0.1 K s^{-1}
Heat-sink diameter	1.5 km	2.1 km (*x* direction), 0.7 km (*y* direction)
Heat-sink depth	Surface–2.8 km AGL	Surface–2.8 km AGL
Base state	Resting, dry, dry-adiabatic	Resting, dry, dry-adiabatic
Lower boundary condition	Semi-slip	Semi-slip

REFERENCES

Barcilon, A. I., 1967: Vortex decay above a stationary boundary. *J. Fluid Mech.*, **27**, 155–175, https://doi.org/10.1017/S0022112067000114.

Batchelor, G. K., 2002: *An Introduction to Fluid Dynamics*. Cambridge University Press, 615 pp.

Boyer, C. H., and J. M. L. Dahl, 2020: The mechanisms responsible for large near-surface surface vertical vorticity within simulated supercells and quasi-linear storms. *Mon. Wea. Rev.*, **148**, 4281–4297, https://doi.org/10.1175/MWR-D-20-0082.1.

Bryan, G. H., and J. M. Fritsch, 2002: A benchmark simulation for moist nonhydrostatic numerical models. *Mon. Wea. Rev.*, **130**, 2917–2928, https://doi.org/10.1175/1520-0493(2002)130<2917:ABSFMN>2.0.CO;2.

Burggraf, O. R., K. Stewartson, and R. Belcher, 1971: Boundary layer induced by a potential vortex. *Phys. Fluids*, **14**, 1821–1833, https://doi.org/10.1063/1.1693691.

Carroll, J. J., and J. A. Ryan, 1970: Atmospheric vorticity and dust devil rotation. *J. Geophys. Res.*, **75**, 5179–5184, https://doi.org/10.1029/JC075i027p05179.

Dahl, J. M. L., 2020: Near-surface vortex formation in supercells from the perspective of vortex patch dynamics. *Mon. Wea. Rev.*, **148**, 3533–3547, https://doi.org/10.1175/MWR-D-20-0080.1.

——, M. D. Parker, and L. J. Wicker, 2012: Uncertainties in trajectory calculations within near-surface mesocyclones of simulated supercells. *Mon. Wea. Rev.*, **140**, 2959–2966, https://doi.org/10.1175/MWR-D-12-00131.1.

——, ——, and ——, 2014: Imported and storm-generated near-ground vertical vorticity in a simulated supercell. *J. Atmos. Sci.*, **71**, 3027–3051, https://doi.org/10.1175/JAS-D-13-0123.1.

Davies-Jones, R., 2002: Linear and nonlinear propagation of supercell storms. *J. Atmos. Sci.*, **59**, 3178–3205, https://doi.org/10.1175/1520-0469(2003)059<3178:LANPOS>2.0.CO;2.

——, and H. Brooks, 1993: Mesocyclogenesis from a theoretical perspective. *The Tornado: Its Structure, Dynamics, Prediction, and Hazards*, *Geophys. Monogr.*, Vol. 79, Amer. Geophys. Union, 105–114, https://doi.org/10.1029/GM079p0105.

Davies-Jones, R. P., 1982: Observational and theoretical aspects of tornadogenesis. *Intense Atmospheric Vortices*, Springer, 175–189.

Deardorff, J. W., 1980: Stratocumulus-capped mixed layers derived from a three-dimensional model. *Bound.-Layer Meteor.*, **18**, 495–527, https://doi.org/10.1007/BF00119502.

Fiedler, B. H., and K. M. Kanak, 2001: Rayleigh-Bénard convection as a tool for studying dust devils. *Atmos. Sci. Lett.*, **2**, 104–113, https://doi.org/10.1006/asle.2001.0046.

Fischer, J., and J. M. L. Dahl, 2020: The relative importance of updraft and cold pool characteristics in supercell tornadogenesis using highly idealized simulations. *J. Atmos. Sci.*, **77**, 4089–4107, https://doi.org/10.1175/JAS-D-20-0126.1.

——, and ——, 2022: Transition of near-ground vorticity dynamics during tornadogenesis. *J. Atmos. Sci.*, **79**, 467–483, https://doi.org/10.1175/JAS-D-21-0181.1.

——, ——, B. E. Coffer, J. L. Houser, P. M. Markowski, M. D. Parker, C. C. Weiss, and A. Schueth, 2024: Supercell tornadogenesis: Recent progress in our state of understanding. *Bull. Amer. Meteor. Soc.*, **105**, E1084–E1097, https://doi.org/10.1175/BAMS-D-23-0031.1.

Giersch, S., and S. Raasch, 2023: How do dust devil-like vortices depend on model resolution? A grid convergence study using large-eddy simulation. *Bound.-Layer Meteor.*, **187**, 703–742, https://doi.org/10.1007/s10546-023-00792-3.

Hess, G. D., and K. T. Spillane, 1990: Characteristics of dust devils in Australia. *J. Appl. Meteor.*, **29**, 498–507, https://doi.org/10.1175/1520-0450(1990)029<0498:CODDIA>2.0.CO;2.

Ito, J., R. Tanaka, H. Niino, and M. Nakanishi, 2010: Large eddy simulation of dust devils in a diurnally-evolving convective mixed layer. *J. Meteor. Soc. Japan*, **88**, 63–77, https://doi.org/10.2151/jmsj.2010-105.

——, H. Niino, and M. Nakanishi, 2013: Formation mechanism of dust devil–like vortices in idealized convective mixed layers. *J. Atmos. Sci.*, **70**, 1173–1186, https://doi.org/10.1175/JAS-D-12-085.1.

Jeong, J., and F. Hussain, 1995: On the identification of a vortex. *J. Fluid Mech.*, **285**, 69–94, https://doi.org/10.1017/S0022112095000462.

Jiménéz, P. A., J. Dudhia, J. F. González-Rouco, J. Navarro, J. P. Montávez, and E. García-Bustamente, 2012: A revised scheme for the WRF surface layer formulation. *Mon. Wea. Rev.*, **140**, 898–918, https://doi.org/10.1175/MWR-D-11-00056.1.

Kanak, K. M., D. K. Lilly, and J. T. Snow, 2000: The formation of vertical vortices in the convective boundary layer. *Quart. J. Roy. Meteor. Soc.*, **126**, 2789–2810, https://doi.org/10.1002/qj.49712656910.

Kurgansky, M. V., A. Montecinos, V. Villagran, and S. M. Metzger, 2011: Micrometeorological conditions for dust-devil occurrence in the Atacama Desert. *Bound.-Layer Meteor.*, **138**, 285–298, https://doi.org/10.1007/s10546-010-9549-1.

Markowski, P., and Y. Richardson, 2010: *Mesoscale Meteorology in Midlatitudes*. John Wiley and Sons, 407 pp.

Markowski, P. M., and Y. P. Richardson, 2014: The influence of environmental low-level shear and cold pools on tornadogenesis: Insights from idealized simulations. *J. Atmos. Sci.*, **71**, 243–275, https://doi.org/10.1175/JAS-D-13-0159.1.

Markowski, P., Y. Richardson, and G. Bryan, 2014: The origins of vortex sheets in a simulated supercell thunderstorm. *Mon. Wea. Rev.*, **142**, 3944–3954, https://doi.org/10.1175/MWR-D-14-00162.1.

Ohno, H., and T. Takemi, 2010: Mechanisms for intensification and maintenance of numerically simulated dust devils. *Atmos. Sci. Lett.*, **11**, 27–32, https://doi.org/10.1002/asl.249.

Okubo, A., 1970: Horizontal dispersion of floatable particles in the vicinity of velocity singularities such as convergences. *Deep-Sea Res. Oceanogr. Abstr.*, **17**, 445–454, https://doi.org/10.1016/0011-7471(70)90059-8.

Parker, M. D., 2023: How well must surface vorticity be organized for tornadogenesis? *J. Atmos. Sci.*, **80**, 1433–1448, https://doi.org/10.1175/JAS-D-22-0195.1.

——, and J. M. L. Dahl, 2015: Production of near-surface vertical vorticity by idealized downdrafts. *Mon. Wea. Rev.*, **143**, 2795–2816, https://doi.org/10.1175/MWR-D-14-00310.1.

Raasch, S., and T. Franke, 2011: Structure and formation of dust devil–like vortices in the atmospheric boundary layer: A high-resolution numerical study. *J. Geophys. Res.*, **116**, D16120, https://doi.org/10.1029/2011JD016010.

Rafkin, S., B. Jemmett-Smith, L. Fenton, R. Lorentz, T. Takemi, J. Ito, and D. Tyler, 2016: Dust devil formation. *Space Sci. Rev.*, **203**, 183–207, https://doi.org/10.1007/s11214-016-0307-7.

Renno, N. O., and Coauthors, 2004: MATADOR 2002: A pilot field experiment on convective plumes and dust devils. *J. Geophys. Res.*, **109**, E07001, https://doi.org/10.1029/2003JE002219.

Rotunno, R., 1980: Vorticity dynamics of a convective swirling boundary layer. *J. Fluid Mech.*, **97**, 623–640, https://doi.org/10.1017/S0022112080002728.

——, 2013: The fluid dynamics of tornadoes. *Annu. Rev. Fluid Mech.*, **45**, 59–84, https://doi.org/10.1146/annurev-fluid-011212-140639.

——, 2014: Secondary circulations in rotating-flow boundary layers. *Aust. Meteor. Oceanogr. J.*, **64**, 27–35, https://doi.org/10.22499/2.6401.004.

——, and J. B. Klemp, 1982: The influence of the shear-induced pressure gradient on thunderstorm motion. *Mon. Wea. Rev.*, **110**, 136–151, https://doi.org/10.1175/1520-0493(1982)110<0136:TIOTSI>2.0.CO;2.

——, and J. Klemp, 1985: On the rotation and propagation of simulated supercell thunderstorms. *J. Atmos. Sci.*, **42**, 271–292, https://doi.org/10.1175/1520-0469(1985)042<0271:OTRAPO>2.0.CO;2.

Shapiro, A., and K. M. Kanak, 2002: Vortex formation in ellipsoidal thermal bubbles. *J. Atmos. Sci.*, **59**, 2253–2269, https://doi.org/10.1175/1520-0469(2002)059<2253:VFIETB>2.0.CO;2.

Simpson, M. W., and A. Glezer, 2016: Buoyancy-induced, columnar vortices. *J. Fluid Mech.*, **804**, 712–748, https://doi.org/10.1017/jfm.2016.541.

Spiga, A., and Coauthors, 2016: Large-eddy simulations of dust devils and convective vortices. *Space Sci. Rev.*, **203**, 245–275, https://doi.org/10.1007/s11214-016-0284-x.

Straka, J., E. Rasmussen, R. P. Davies-Jones, and P. Markowski, 2007: An observational and idealized numerical examination of low-level counter-rotating vortices in the rear flank of supercells. *Electron. J. Severe Storms Meteor.*, **2** (8), https://doi.org/10.55599/ejssm.v2i8.13.

Vande Guchte, A., and J. M. L. Dahl, 2018: Sensitivities of parcel trajectories beneath the lowest scalar model level of a Lorenz vertical grid. *Mon. Wea. Rev.*, **146**, 1427–1435, https://doi.org/10.1175/MWR-D-17-0190.1.

Walko, R. L., 1993: Tornado spin-up beneath a convective cell: Required basic structure of the near-field boundary layer winds. *The Tornado: Its Structure, Dynamics, Prediction, and Hazards*, *Geophys. Monogr.*, Vol. 79, Amer. Geophys. Union, 89–95, https://doi.org/10.1029/GM079p0089.

Weiss, J., 1991: The dynamics of enstrophy transfer in two-dimensional hydrodynamics. *Physica D*, **48**, 273–294, https://doi.org/10.1016/0167-2789(91)90088-Q.

Wu, J.-Z., H.-Y. Ma, and M.-D. Zhou, 2006: *Vorticity and Vortex Dynamics*. Springer, 776 pp.